ELSEVIER

Molecular mechanism of anti-SARS-CoV2 activity of Ashwagandha-derived withanolides

Jaspreet Kaur Dhanjal [a], Vipul Kumar [b], Sukant Garg [c], Chandru Subramani [d], Shubhra Agarwal [d], Jia Wang [c], Huayue Zhang [c], Ashish Kaul [c], Rajkumar Singh Kalra [c], Sunil C. Kaul [c], Sudhanshu Vrati [d,*], Durai Sundar [b,*], Renu Wadhwa [c,*]

[a] Indraprastha Institute of Information Technology Delhi, Okhla Industrial Estate, Phase III, New Delhi 110 020, India
[b] DAILAB, Department of Biochemical Engineering & Biotechnology, Indian Institute of Technology (IIT) Delhi, Hauz Khas, New Delhi 110 016, India
[c] AIST-INDIA DAILAB, DBT-AIST International Center for Translational & Environmental Research (DAICENTER), National Institute of Advanced Industrial Science & Technology (AIST), Tsukuba 305 8565, Japan
[d] Regional Centre for Biotechnology (RCB), Faridabad 121 001, India

ARTICLE INFO

ABSTRACT

COVID-19 caused by SARS-CoV-2 corona virus has become a global pandemic. In the absence of drugs and vaccine, and premises of time, efforts and cost required for their development, natural resources such as herbs are anticipated to provide some help and may also offer a promising resource for drug development. Here, we have investigated the therapeutic prospective of Ashwagandha for the COVID-19 pandemic. Nine withanolides were tested *in silico* for their potential to target and inhibit (i) cell surface receptor protein (TMPRSS2) that is required for entry of virus to host cells and (ii) viral protein (the main protease M^{pro}) that is essential for virus replication. We report that the withanolides possess capacity to inhibit the activity of TMPRSS2 and M^{pro}. Furthermore, withanolide-treated cells showed downregulation of TMPRSS2 expression and inhibition of SARS-CoV-2 replication *in vitro*, suggesting that Ashwagandha may provide a useful resource for COVID-19 treatment.

1. Introduction

The outbreak of a new strain of coronavirus SARS-CoV-2 in Wuhan, China, in December 2019, the cause of COVID-19, is now a global pandemic that has spread across 213 countries. WHO has reported more than 169,597,415 confirmed cases of COVID-19, including 3,530,582 deaths worldwide as of May 30, 2021 [1]. This global emergency has affected the lives of millions of people, challenged healthcare systems, and hit hard on the global economy. The situation is anticipated to worsen if SARS-CoV-2 spread is not contained, or effective treatments are not developed.

Coronaviruses are grouped into four classes - alpha, beta, gamma and delta, which can infect both humans and animals. Similar to SARS-CoV-2, the previous outbreaks of severe acute respiratory syndrome (SARS-CoV, 2002/2003 in Guangdong, China) and Middle East respiratory syndrome (MERS-CoV, 2012 in Saudi Arabia) were caused by beta coronaviruses [2]. This beta class of coronaviruses is pathogenic for humans, characterized by a single-stranded RNA genome encapsulated by a membrane envelope [3]. The protruding transmembrane spike glycoproteins (S proteins) from the surface of these viruses give them a crown-like morphology and hence the name corona [4]. The infection cycle of coronaviruses starts with their entry into the host cells. The S1 unit of viral glycoprotein first attaches to the host cellular receptor angiotensin-converting enzyme 2 (ACE2). The entry of the virus into the cell further depends upon the S protein priming by the host cellular protease called transmembrane protease serine 2 (TMPRSS2). TMPRSS2 cleaves the S protein at the S1/S2 and the S2' site, and facilitates the fusion of viral particle with the host cellular membrane [5], thus becomes crucial factor for infectivity and propagation of SARS-CoV-2. SARS-CoV-2 can also employ endosomal cysteine proteases CatB/L for the priming of its glycoprotein in cells deficient in TMPRSS2. However, TMPRSS2 but not CatB/L was shown to be essential for the entry and

---

* Corresponding authors.

E-mail addresses: jaspreet@iiitd.ac.in (J.K. Dhanjal), vipul.kumar@dbeb.iitd.ac.in (V. Kumar), sukant.garg@aist.go.jp (S. Garg), s.chandru@rcb.res.in (C. Subramani), shubhra.agarwal@rcb.res.in (S. Agarwal), wang-jia0819@aist.go.jp (J. Wang), zhang-huayue@aist.go.jp (H. Zhang), ashish-kaul@aist.go.jp (A. Kaul), rajkumar-singh@oist.jp (R.S. Kalra), s-kaul@aist.go.jp (S.C. Kaul), vrati@rcb.res.in (S. Vrati), sundar@dbeb.iitd.ac.in (D. Sundar), renu-wadhwa@aist.go.jp (R. Wadhwa).

spread of the viral particles [6]. In another report, Vero E6 cell line was engineered for high expression of TMPRSS2. These cells were found to be highly susceptible to SARS-CoV-2 infection and hence were suggested to be appropriate for isolation and propagation of the virus [7]. Notably, the importance of TMPRSS2 in the process of normal development, growth or organ function has not been established as yet. The knockout of TMPRSS2 in mouse model for cancer research has also been shown to be entirely dispensable with no significant phenotypic alterations [8]. Overexpression of TMPRSS2 and HAT has been previously reported to promote the growth of different subtypes of human and avian influenza viruses [9,10]. In these premises, TMPRSS2 has emerged as a promising target for treatment/prevention of SARS-CoV-2 and other related infections.

After the entry into the host cell, the replicase gene of the viral genome encodes for two overlapping polyproteins, namely pp1a and pp1ab [11,12]. The functional polypeptides required for viral replication and transcription of the viral genome are then released from these polyproteins by extensive proteolytic activity, which is predominantly mediated by the main protease (M^{pro}) of SARS-CoV-2. The M^{pro} (also known as 3C-like protease) cleaves the polyprotein at multiple conserved sites after the autolytic cleavage of itself from pp1a and pp1ab [13]. The importance of M^{pro} in the infection cycle of virus and absence of proteins homologous to this enzyme in the host cell, make M^{pro} also an attractive target for developing antiviral therapies [14]. M^{pro} from different human and animal coronaviruses possess high similarity in terms of primary amino acid sequence and the functional tertiary structure. The antiviral drugs designed for M^{pro} are mainly targeted to its highly conserved substrate binding pocket [15]. Similar to other coronaviruses, SARS-CoV-2 also shares this homology in its M^{pro} enzyme. Several key identical residues at the various sub-sites of substrate binding pocket of M^{pro} of different coronaviruses including SARS-CoV-2 have been reported [16]. These conserved residues mainly include His41, Tyr54, His163, Glu166, His172, Asp187 and Gln192.

Various strategies to inhibit TMPRSS2 and M^{pro}, and its potential for management of COVID-19 have been reported and discussed here. Peptide-conjugated phosphorodiamidate morpholino oligomers that sterically blocked TMPRSS2 transcription has been reported to significantly suppress the viral titers [17]. BAPA (benzylsulfonyl-d-arginine-proline-4-amidinobenzylamide), a potent inhibitor of HAT and TMPRSS2 has also been shown to strongly affect the virus propagation [18,19]. Camostat mesylate, a clinically proven and commercially available serine protease inhibitor, in use for the treatment of oral squamous cell carcinoma [20], dystrophic epidermolysis [21], exocrine pancreatic enzyme inhibition [22,23], and chronic pancreatitis [24,25], has also been suggested as a candidate antiviral drug. It has been shown to suppress infection of SARS-CoV and human coronavirus NL63 in HeLa cells that express ACE2 and TMPRSS2 proteins [26]. Camostat was shown to partially block the entry of MERS-CoV into TMPRSS2 expressing Vero cells, effect of which was enhanced on the simultaneous use of inhibitors of cathepsin L. Of note, Camostat was shown to suppress the entry of MERS-CoV into Calu-3 cells by 10-fold that led to 270-fold decrease in virus titer [27]. Most recently, Camostat mesylate was shown to block the entry of SARS-CoV-2 into the cells [5]. Many antiviral drugs have also been proposed in the past against the M^{pro} enzyme of different coronaviruses, however, many candidates have now been successfully identified and shown to inhibit the M^{pro} of SARS-CoV-2. A series of candidate drugs, mainly derived from the already known inhibitors, have been co-crystallized with SARS-CoV-2 protease [28,29]. Crystal structure of SARS-CoV-2 M^{pro} bound to X77 and baicalein as inhibitors is also available at PDB ID- 6W63 and 6M2N, respectively. Repurposing of approved drugs and clinical candidates has also led to the identification of six small molecules, ebselen, disulfiram, carmofur, tideglusib, shikonin and PX-12, as inhibitors of SARS-CoV-2 M^{pro} [30]. Lopinavir and Ritonavir, found to be effective in adults with severe COVID-19 symptoms [31], were also shown to be targeting the main protease of SARS-CoV-2 [32].

Ashwagandha (*Withania somnifera*), an Indian Ayurvedic herb, is known for its therapeutic activities and potential to boost the body immunity. Withaferin-A (Wi-A), a bioactive steroidal lactone from Ashwagandha, has been shown to be capable of inhibiting herpes simplex virus and suppress HIV-1 LTR transcription and viral replication [33,34]. Wi-A has also been predicted to target the neuraminidase of H1N1 influenza virus [35]. We have reported anticancer activity of two withanolides, Wi-A and Withanone (Wi-N) that work through multiple mechanisms, including activation of tumor suppressor proteins, p53 and pRB, inactivation of NF-kB, Aurora A, DNA damage repair and oxidative stress [36–43]. On these premises, we investigated the anti-COVID-19 potential of Wi-A and Wi-N using bioinformatics and experimental tools. We reported that both Wi-A and Wi-N could dock into the catalytic site of TMPRSS2, however, the interactions of Wi-N were stronger than that of Wi-A [44]. By expression analyses of control and Wi-N-treated cells, we found that the latter possess low level of TMPRSS2 mRNA, suggesting that Wi-N has capability to downregulate the expression of TMPRSS2 [44]. We have also reported Wi-N to be a potential inhibitor of SARS-CoV-2 M^{pro} protein [16]. In the present study, we examined the potential of several withanolides for their ability to (i) block the interaction of SARS-CoV-2 with host cells receptor (TMPRSS2) and downregulate the expression of TMPRSS2 at the mRNA and protein levels, and (ii) interact at the substrate binding site of main protease (M^{pro}) of SARS-CoV-2. Among the tested compounds, six withanolides- Withaferin-A, Withanone, Withanolide-A, Withanoside-IV and Withanoside-V significantly inhibited the expression of TMPRSS2 at both transcriptional and translational level. Furthermore, molecular docking and computational analyses predicted that most of these withanolides may also inhibit the M^{pro} of SARS-CoV-2. Anticipating the value of these findings for COVID-19 treatment, we tested their anti-viral potential in a cell-based assay and found that the most withanolides, although to a variable extent (ranging from 17 to 84%) caused inhibition of infection as determined by RT-PCR amplification of viral envelope and nucleocapsid sequences. We also report here that the water-based Ashwagandha extracts, containing a mixture of withanolides, may provide a useful resource for COVID-19 treatment.

2. Methods

2.1. Preparation of protein and ligands structure for molecular docking

The crystal structure of TMPRSS2 is not yet available in the Protein Data Bank, hence its modeled structure was retrieved from the Swiss model repository (ID: O15393). The structure was modeled based on another homologous Transmembrane class II family protein, Serine protease hepsin. The identity between the sequence of TMPRSS2 and hepsin is 33.82%, and the Q mean of the modeled structure has been reported to be −1.62, which is an indicative of a good quality modeled structure. The catalytic domain in both the proteins was found to be well conserved with His296, Asp345 and Ser441 as functional residues [45]. Further, the structure of M^{pro} complexed with a peptide-like inhibitor N3 was retrieved from the PDB (6LU7) [30]. These structures were optimized and prepared for docking studies using the protein preparation wizard of the Schrodinger suite [46]. Preparation of the structure included the removal of water molecules, addition of polar hydrogen atoms, filling of missing amino acid side chains and minimization of the structure using the OPL3e force field [47].

The structure of Camostat mesylate (CID-5284360) and various withanolides- Withaferin-A (CID-265237), Withanone (CID-21679027), Withanoside-V (CID-10700345), Methoxy Withaferin-A (CID-10767792), Withanolide-A (CID-11294368), Withanolide-B (CID-14236711), 12-deoxywithastramonolide (CID-44576309) and Withanoside-IV (CID- 71312551), as shown in Supplementary Fig. 1, were retrieved from PubChem and prepared for docking using the LigPrep tool of the Schrodinger suite [46,48]. This preparation mainly included the generation of ionization states at pH 7 ± 2 using the Epik

program, desalting of the ligands, generation of tautomers and stereo-isomers while retaining the specific chiralities and minimization of the generated ligand structures using OPL3e forcefield [47,49].

2.2. Molecular docking of the ligands with TMPRSS2

The key catalytic residues of TMPRSS2 involved in the proteolytic activity have been reported as His296, Asp345 and Ser441 [50,51]. The 20 Å^3 grid for docking with TMPRSS2 was generated taking its catalytic residues- His296, Asp345 and Ser441 as the centroid. In case of M^{pro}, the grid of 20 Å^3 was generated by covering the residues making polar contacts with N3 inhibitor in the native crystal structure of M^{pro} that mainly involved Phe140, Asn142, Gly143, His164 and Glu166. The Glide module of Schrodinger was used for the extra precision (XP) flexible docking of the ligands at the generated grid sites [46,52].

2.3. Explicit water molecular dynamics (MD) simulation and its analysis

To investigate the stability of binding and interactions between the proteins and ligands, the docked complexes were subjected to MD simulations. The MD simulations were done using the Desmond tool integrated with the maestro of the Schrodinger suite [46,47,53]. Firstly, the systems were built, in which the docked complexes were solvated with TIP3P water model. Appropriate number of ions (Na^+/Cl^-) were then added to neutralize these systems enclosed in the orthorhombic periodic boundary boxes. The energy of the prepared systems was minimized by running 100 ps low-temperature ($10K$) Brownian motion MD simulation in NVT ensemble to remove steric clashes and move the system away from an unfavourable high-energy conformation. The systems were further relaxed using default parameters of 'relax system before simulation' option of Desmond. The equilibrated systems were then subjected to 100 ns simulation in NPT ensemble with 300 K temperature maintained by Nose–Hoover chain thermostat, constant pressure of 1 atm maintained by Martyna–Tobias–Kelinbarostat, the time step of 2 fs, and recording interval of 20 ps.

The generated MD simulation trajectories were visualized and analyzed using the system event analysis and simulation interaction diagram tools. To account for the stability of the simulated complexes, the global deviation or the Root Mean Square Deviation (RMSD) in the structures with reference to initial docked structures throughout the simulation run was analyzed. The Root Mean Square Fluctuation (RMSF) was also calculated to investigate the average fluctuation in the amino acid residues of the apo proteins and their complexes with different ligands. As hydrogen bonds are crucial in determining the specificity and affinity of a drug towards its receptor, we next calculated the average number of the hydrogen bonds formed during the simulation time for each protein-ligand complex [54]. Furthermore, to investigate the significant interactive residues of the proteins, which were making contact with the ligands during the MD simulation, the polar and non-polar interactions, as well as the occupancy time of those interactions was calculated. Finally, the MM/GBSA (molecular mechanics energies combined with the generalized Born and surface area continuum solvation) free binding energy was calculated using the prime module of the Schrodinger suite [46,55] to determine the binding affinity of the ligands towards the target proteins. A hundred frames equally spanned between 40 and 100 ns of the trajectory were used for this computation using the following equation:

$$MM/GBSA\ \Delta G_{bind} = \Delta G_{complex} - \left(G_{receptor} + G_{ligand}\right)$$

$$\Delta G = \Delta E_{gas} + \Delta G_{sol} - T\Delta S_{gas}$$

$$\Delta E_{gas=}\ \Delta E_{int} + \Delta E_{elec} + \Delta E_{vdw}$$

$$\Delta G_{sol} = \Delta G_{gb} + \Delta G_{surf}$$

The prime module of Schrodinger software was used to compute all

the energy components using the coordinates of complex, receptor and ligand using OPL3e forcefield. The binding free energy (ΔG_{bind}) can be dissociated into the binding free energy of the complex ($\Delta G_{complex}$), receptor ($\Delta G_{receptor}$) and ligand (ΔG_{ligand}). The gas-phase interaction energy (ΔE_{gas}) was calculated as the sum of electrostatic (ΔE_{elec}) and van der waal (ΔE_{vdw}) interaction energies, while internal energy term was neglected. The solvation free energy (ΔG_{sol}) contains non-polar (ΔG_{surf}) and polar solvation energy (ΔG_{gb}), which was calculated using the VSGB solvation model and OPL3e force field, neglecting the entropy factor.

2.4. Cell culture and treatments

Human-derived esophageal squamous carcinoma (T.Tn), human breast carcinoma (MCF7), non-small lung cancer (A549), and tongue oral squamous carcinoma (HSC3) cell lines were procured from the Japanese Collection of Research Bioresources (JCRB) Cell Bank, Japan. Vero E6 cells were procured from the National Centre for Cell Science (NCCS), Pune, India. Cells were cultured in Gibco Dulbecco's Modified Eagle Medium (DMEM)- supplemented with 2–10% fetal bovine serum and 1% penicillin/streptomycin in a humidified incubator (37 °C and 5% CO_2). Cells were treated with non-toxic doses of the test reagents as determined by independent viability experiments for each cell line.

2.5. Cell viability assay

Cytotoxicity of the various withanolides was tested in T.Tn and other cells using MTT (3-(4,5-dimethylthiazol-2-yl)-2,5-diphenyltetrazolium bromide) assay. Five thousand cells per well were plated in a 96-well plate, allowed to settle overnight, and treated with each compound. The control (DMSO) or treated cells were incubated for 48 h followed by the addition of 10 μL of phosphate-buffered saline (PBS) containing 5 mg/mL MTT (M6494, Life Technologies, Carlsbad, CA, USA), and further incubated for 4 h. The culture medium containing MTT was then aspirated and replaced with DMSO. The plates were placed on a shaker for 5 min followed by measurement of optical density at 570 nm using Tecan infinite M200 Pro microplate reader (Tecan Group Ltd., Mannedorf, Switzerland). Cell viability was calculated as a percentage against the control to identify their inhibitory concentration (IC) value using Microsoft™ Office 2016. Statistical significance was calculated by an unpaired *t*-test of Microsoft Excel software (2016).

2.6. Quantitative cell viability (QCV) assay

2.6.1. Short-term QCV
A total of 1×10^5 cells per well were plated in a 12-well plate and allowed to settle overnight, followed by treatment with each of the withanolides. The control or treated cells were incubated at 37 °C and 5% CO_2. After 48 h, cells were fixed with acetone: methanol (1:1), stained with Crystal Violet (CV), and de-stained into the solution, which was quantified by the help of a spectrophotometer at 570 nm. Statistical significance was calculated by an unpaired *t*-test of Microsoft Excel® software (2016).

2.6.2. Long-term QCV
100 cells per well were plated in a 12-well plate and allowed to settle overnight, followed by treatment with each of the withanolides. The control or treated cells were incubated at 37 °C and 5% CO_2, and the withanolide-supplemented medium was replaced every alternate day. After 9 days, cells were fixed, stained, and de-stained into the solution, which was quantified by the help of a spectrophotometer as described in the earlier section. Statistical significance was calculated by an unpaired *t*-test of Microsoft Excel software (2016).

2.7. Reverse transcription - polymerase chain reaction (RT-PCR)

A total of 2×10^5 cells per well were plated in a 6-well plate, allowed

to settle overnight, followed by treatment with each of the withanolides. The control or treated cells were incubated at 37 °C and 5% CO$_2$. After 48 h, the cells were harvested from the petri dishes and lysed with Trizol (Ambion®, Foster City, CA, USA, 15596018) at room temperature for 5 min, segregated in chloroform (Wako, Tokyo, Japan, 038–02606) at room temperature for 5 min, centrifuged at 12,000 rpm for 15 min and supernatant was separated. The supernatant was then washed in iso-propanol (Wako, 166-04836) at room temperature for 10 min, centrifuged at 12,000 rpm for 15 min and pellet was washed in 70% ice-cold ethanol and centrifuged at 8000 rpm for 5 min twice, followed by air-drying and resuspension in nuclease-free water to extract the pure RNA. The concentration and quality of RNA was evaluated through a spectrophotometer (ND-1000, Nanodrops, Wilmington, NC, USA). The cDNA was prepared using a reverse transcription kit (Qiagen, Hilden, Germany, 205,313) following the manufacturer's instructions. The master mix for amplification was prepared by mixing 1 μL cDNA with 0.1 μL Ex Taq (Takara, Kusatsu, Shiga, Japan, RR001), 2 μL 10× TAQ buffer, 2 μL dNTP, 1 μL each of forward and reverse primers (indicated earlier) in 12.9 μL nuclease free water and amplified using 'denaturation = 95°C, 10 min ➔ amplification = 95°C, 45s - 60°C, 1 min - 72°C, 45s (35~37 cycles) ➔ annealing = 72°C, 10min ➔ 4°C' protocol. The amplified products were resolved on a 1% agarose gel containing 0.0625 μg/mL EtBr (Ethidium Bromide; Invitrogen, 15,585–011), and image was acquired using a Lumino Image Analyzer (LAS3000-mini; Fuji Film, Tokyo, Japan) equipped with a CCD (charge-coupled device) camera. Band intensity was quantified using ImageJ software (NIH) and plotted as a percentage using Microsoft™ Office 2016. Statistical significance was calculated by an unpaired *t*-test of Microsoft Excel 2016. The details of primers used are:

TMPRSS2: F'–GAGGACGAGAATCGGTGTGT, R'–TCCAGTCGTCT TGGCACA; 103bp; Tm- 61°C;

GAPDH: F'–TGGAAATCCCATCACCATCT, R'–TTCACACCCA TGACGAACAT; 417bp; Tm- 60°C.

2.8. Western blotting

A total of 2.5×10^5 cells per well were plated in a 6-well plate, allowed to settle overnight, followed by treatment with each of the withanolides. The control or treated cells were incubated at 37 °C and 5% CO$_2$. After 48 h, control and treated cells were harvested and washed twice with PBS, followed by lysis in RIPA buffer (89,900, Thermo Fisher Scientific) containing complete protease inhibitor cocktail (4,693,159,001, Roche Applied Science, Penzberg, Bavaria, Germany) on ice for 45 min. Lysates were separated on an SDS-polyacrylamide gel using Mini-Protean® Tetra cell equipment (Bio-Rad, Hercules, CA, USA) and subjected to western blotting using protein-specific primary antibodies [anti-TMPRSS2 (AbCam ab92323), anti-β-actin (AbCam ab49900)], and horseradish peroxidase-conjugated secondary HRP antibody (31,430 or 31,460, Thermo Fisher Scientific). Blots were developed using chemiluminescence solution (GE Healthcare, Buckinghamshire, UK) and visualized using a Lumino Image Analyzer (LAS 3000-mini; Fuji Film, Tokyo, Japan). Band intensity was quantified using ImageJ software (NIH) and plotted as a percentage using Microsoft™ Office 2016.

2.9. Immunostaining

Cells (5×10^4) were seeded on 18-mm glass coverslips, placed in 12-well plates and cultured for 24 h in a humidified incubator (37 °C and 5% CO$_2$) for attachment. The cells were then treated with the withanolides or extracts for 24 h. The cells were then washed with PBS and fixed with methanol: acetone (1:1) at 4 °C for 10 min. After that, fixation solution was removed, and cells were again washed with PBS and permeabilized by PBST for 10 min. After permeabilization, the glass coverslips were blocked for an hour with 2% bovine serum albumin in PBST. The coverslips were then incubated overnight at 4 °C with anti-

TMPRSS2 primary antibodies [AbCam (ab92323)]. Protein localization and expression were visualized by secondary staining with either Alexa Flour-488 conjugated Goat Anti-rabbit IgG (Catalogue#A-11034) or Alexa Flour-546 conjugated Goat Anti-rabbit (Catalogue#A-11035) antibody. After the incubation with secondary antibody, cells were washed with PBST for 10 min followed by nuclear counter staining with Hoechst 33342 (Molecular Probes, Oregon, U.S.A.). The cells were again washed with PBST for 10 min, followed by PBS washing for 10 min, and afterwards, a Milli-Q H$_2$O wash for 10 min. Finally, the cells were mounted in FA mounting solution (VMRD, Inc., WA, U.S.A.) and examined using a Zeiss Axiovert 200 M immunofluorescence microscope and analyzed by AxioVision 4.6 software (Carl Zeiss, Oberkochen, Germany).

2.10. Anti-viral activity assay

The assay was done in a 96-well plate in triplicates for each sample. A total of 1×10^4 Vero E6 (kidney epithelial cells from *Cercopithecus aethiops*, ATCC) cells were plated per well and incubated at 37 °C overnight for the monolayer formation. Cells were incubated with the culture medium with the test substance (dissolved in DMSO) at a non-cytotoxic concentration of 5–10 μM and the final DMSO concentration of 0.5%. This was followed by the addition of SARS-CoV-2 (USA-WA1/2020 strain) at a 0.01 multiplicity of infection. Control cells were incubated with culture medium with 0.5% DMSO. Plates were incubated at 37 °C and culture supernatant harvested at 24 h and 48 h later. Viral RNA was isolated from 100 μl cell culture supernatant using PureLink Viral RNA/DNA Mini Kit (Invitrogen). cDNA was prepared using ImProm-II Reverse Transcription System (Promega). Real-time PCR was performed in QuantStudio 6 Flex Real-Time PCR System using TB Green Premix Ex Taq II (TaKaRa). The following primers were used to quantify viral RNA levels: (a) Envelope (E) primers FP 5'-ACAGGTACGTTAA-TAGTTAATAGCGT-3' RP 5'- ATATTGCAGCAGTACGCACACA-3' (b) Nucleocapsid (N) primers FP 5'-GACCCCAAAATCAGCGAAAT-3' RP-5'-TCTGGTTACTGCCAGTTGAATCTG-3'. The Ct values for N and E gene sequence detection were determined and used for calculating the percent virus inhibition with respect to the control.

2.11. Statistical analyses

Statistical significance was calculated by an unpaired *t*-test of GraphPad software (2018–2019) (GraphPad, San Diago, CA, USA) using mean, SD (standard deviation), and N (number) from three independent experiments, and shown as $*p < 0.05$, $**p < 0.01$, $***p < 0.001$ or ns = not significant.

3. Results

In order to explore the therapeutic potential of Ashwagandha in the current COVID-19 pandemic, we considered host cell surface protein TMPRSS2, which facilitates the process of virus entry to the cells, as the target. Ashwagandha-derived nine withanolides were examined for their ability to (a) interact with/block, and (b) reduce TMPRSS2 expression using (i) molecular docking and computational analyses, and (ii) mRNA and protein expression in control and withanolide-treated cells, respectively.

3.1. Binding affinity of withanolides towards TMPRSS2 predicted Withanoside-V and Withanoside-IV as the best among all the withanolides

Camostat mesylate is a known inhibitor of TMPRSS2. It was thus used as a reference molecule for molecular docking analysis. At first, we estimated the binding affinity of Camostat mesylate at the catalytic site of TMPRSS2; the docking score in the best binding pose was found to be −5.90 kcal/mol. Among the different non-bonded interactions, only one hydrogen bond was observed with Gly464 of TMPRSS2. Next,
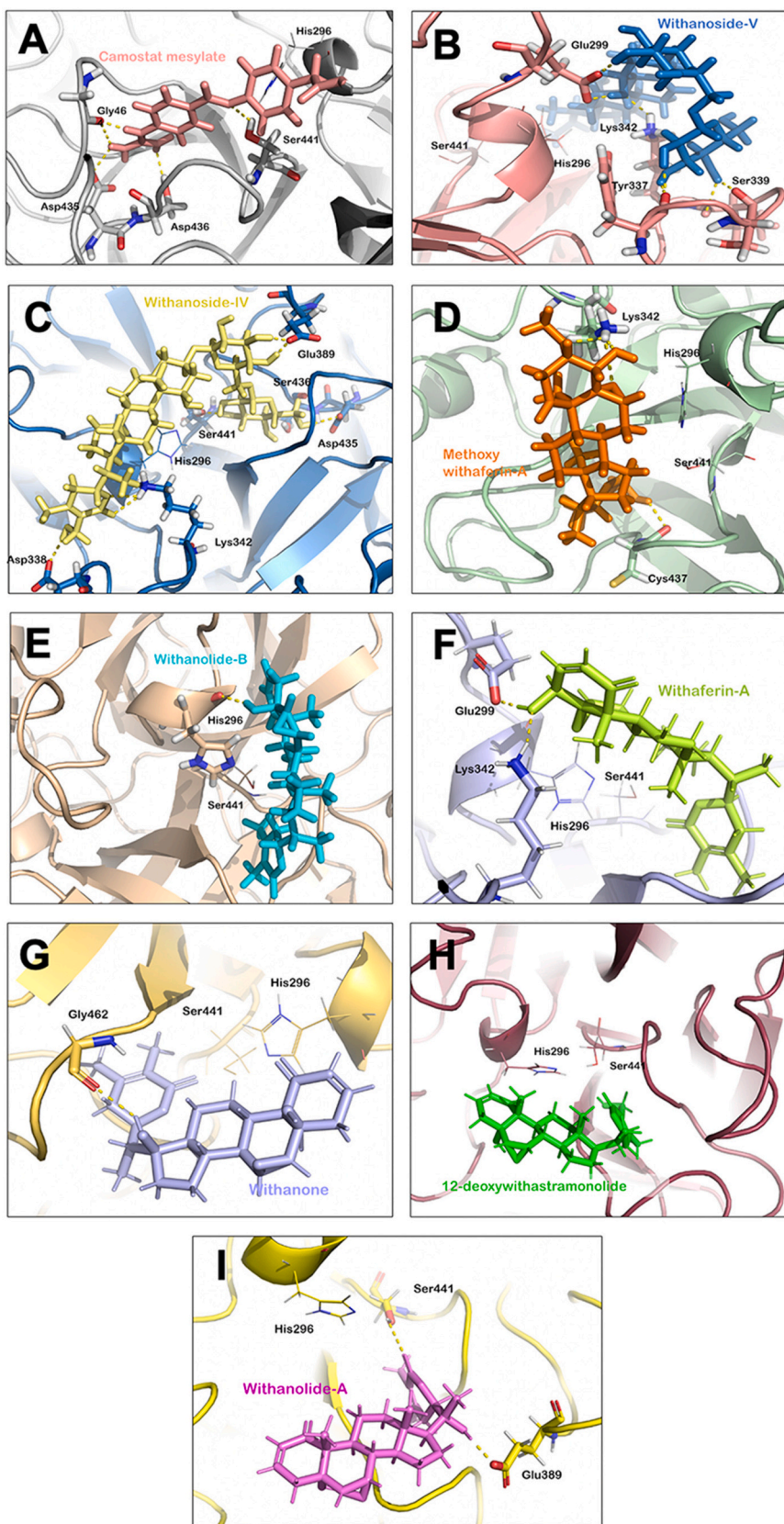
Fig. 1. Interactions of TMPRSS2 residues with the ligands in the best docked pose. (A) TMPRSS2-Camostat mesylate (B) TMPRSS2-Withanoside-V (C) TMPRSS2-Withanoside-IV (D) TMPRSS2-Methoxy Withaferin-A (E) TMPRSS2-Withanolide-B (F) TMPRSS2-Withaferin-A (G) TMPRSS2-Withanone (H) TMPRSS2-12-deoxywithastramonolide (I) TMPRSS2-Withanolide-A.

Table 1

TMPRSS2 residues interacting with the ligands in their best docked pose.

Complex	Molecular docking (kcal/mol)	Types of interactions and residues involved (Pre-molecular dynamic simulations)	
		H-bonds	Hydrophobic, polar and pi-pi stacking
TMPRSS2-Camostat mesylate	−5.90	Gly464	Val275, Gln276, Val278, Val 280, His296, Cys297, Leu302, Asp435, Ser436, Cys437, Gln438, Gly439, Ser441, Thr459, Trp461, Gly462, Cys465, Ala466, Gly472, Val473
TMPRSS2-Withaferin-A	−5.60	Glu299, Lys342	His296, Tyr337, Glu389, Asp435,, Asp435, Ser436, Cys437, Gln438, Asp440, Ser441, Thr459, Ser460, Trp461, Gly462, Ser463. Gly464, Cys465, Ala466, Gly472
TMPRSS2-Withanone	−4.30	Gly462	His296, Glu299, Tyr337, Lys342, Glu389, Asp435, Ser436, Cys437, Gln438, Ser441, Thr459,Ser460, Trp461, Ser463, Gly464, Cys465, Gly472, Val473
TMPRSS2-Withanoside-V	−7.96	Glu299, Tyr337, Ser339	His296, Lys300, Tyr337, Asp338, Lys340, THr341, Lys342, Asp435, Ser436, Cys437, Gln438, Gly439, Ser441, Thr459, Ser460, Trp461, Gly462, Gly464, Cys465, Gly472, Val473
TMPRSS2- Withanoside-IV	−6.92	Asp338, Lys342, Glu389, Ser436, Ser441	His296, Glu299, Tyr337, Asp435, Cys437, Gln438, Gly439, Asp440, Thr459, Ser460, Trp461, Gly462, Gly464, Cys465, Ala466, Gly472, Val473
TMPRSS2- Methoxy Withaferin-A	−4.35	Lys342, Ser436, Cys437	His296, Glu299, Tyr337, Asp435, Gln438, Asp440, Ser441, Thr459, Ser460, Trp461, Gly462, Gly464, Cys465, Ala466, Gly472, Val473
TMPRSS2- Withanolide-B	−4.29	His296	Val280, Cys281, Cys297, Leu302, Glu389, Ser436, Cys437, Gln438, Gly439, Ser441, Thr459, Ser460, Trp461, Gly462, Gly464, Cys465, Ala466, Gly472, Val473
TMPRSS2-Withanolide-A	−4.26	Glu389	His296, Leu419, Ly342, Ser436, Cys437, Gln438,

Table 1 (*continued*)

Complex	Molecular docking (kcal/mol)	Types of interactions and residues involved (Pre-molecular dynamic simulations)	
		H-bonds	Hydrophobic, polar and pi-pi stacking
TMPRSS2-12-deoxywithastramonolide			Gly439, Ser441, Thr459, Ser460, Trp461, Gly462, Gly464, Cys465

−4.04–His296, Glu299, Ly342, Ser436, Cys437, Gln438, Gly439, Ser441, Thr459, Ser460, Trp461, Gly462, Gly464, Cys465

Withaferin-A, Methoxy Withaferin-A, Withanone, Withanolide-A, Withanolide-B, Withanoside-IV, Withanoside-V and 12-deoxywithastramonolide were docked at the same catalytic site of TMPRSS2. The best docking pose for each with hydrogen bonded interactions is shown in Fig. 1. Among these, Withanoside-IV and Withanoside-V had a docking score better than that of Camosat mesylate, while the docking score for the other compounds was also comparable. The binding score for Withanoside-IV and TMPRSS2 complex was −6.92 kcal/mol. On the other hand, TMPRSS2-Withanoside-V complex had a docking score of −7.96 kcal/mol in the best binding pose. The details of molecular interactions (polar and non-polar) for all the complexes with their docking scores are shown in Table 1. The docked complexes were simulated in an explicit water environment to assess the dynamic behaviour of the interactions between protein and ligands. Despite a good docking score, the binding of Withanolide-A and 12-deoxywithastramonolide with TMPRSS2 was found to be unstable in molecular dynamics simulations. The ligands moved out from the catalytic pocket of TMPRSS2 within 50 ns of the simulation run. All other compounds were found to be interacting stably throughout the 100 ns of the MD simulation, similar to Camostat mesylate (Supplementary Fig. 2A). The overall conformation of the docked complexes also did not deviate much from their original docked pose, as inferred from the RMSD plot (Supplementary Fig. 2B). The RMSF plot of the complexes was found to be similar to TMPRSS2 (Apo) residues, where no significant fluctuation was found in the catalytic triad. The fluctuations were observed only in the outer loop region, Pro335 to Lys340 of the protease enzyme (Supplementary Fig. 2C). No significant change in secondary structure conformation as well as global structure was seen due to the binding of these ligands with TMPRSS2 when compared with the Apo form. The hydrogen bond interactions strongly influence the specificity, metabolization, and absorption of the drugs and are considered a reliable measure for drug design [54]. So, we next calculated the number of hydrogen bonds formed between the protein-ligand complexes throughout the simulation run. Withanoside-IV formed the highest number of hydrogen bonds, followed by Camostat mesylate, Withanoside-V, Withanolide-B, and Methoxy Withaferin-A as shown in Fig. 2A. All the ligands except Methoxy Withaferin-A, showed binding in the same binding pocket and interacted with similar residues in the best docked pose. Furthermore, various other ligand properties bound to the protein were also calculated to analyze their binding stability, compactness and solvent accessibility. All properties of these ligands were found to be comparable with each other, and all the calculations with the average values and standard deviation throughout the 100 ns of the simulations are shown in Supplementary Table 1. The consistency and the number of polar as well as non-polar interactions play a crucial role in drug specificity and affinity towards the target protein. Hence, we next analyzed the number of residues and their occupancy in interactions throughout the simulations. Mainly four kinds of interactions were calculated, namely, hydrogen bonding, hydrophobic contacts such as pi-cation and pi-pi contacts, and ionic interactions between two oppositely charged residues. While analyzing these interactions, it was found that all the compounds were making

Fig. 2. The analysis of the Molecular Dynamics (MD) simulations of TMPRSS2 with Camostat mesylate and Ashwagandha derived withanolides. The comparison of number of hydrogen bond counts throughout the simulations showing Withanoside-V to have the highest hydrogen bond interactions with TMPRSS2 (A). The occupancy of TMPRSS2 residues while making polar and non-polar interactions with Camostat mesylate and different withanolides as observed over the entire simulation trajectory. (B) TMPRSS2-Withanoside-IV (C) TMPRSS2-Camostat mesylate (D) TMPRSS2-Withanoside-V (E) TMPRSS2-Methoxy Withaferin-A (F) TMPRSS2-Withanolide-B (G) TMPRSS2-Withaferin-A (H) TMPRSS2-Withanone.

Table 2

Residues of TMPRSS2 interacting with the ligands during the course of MD simulations along with the free binding energy of each protein-ligand complex.

Complex	MMGBSA free binding energy (kcal/mol)	Types of interactions and residues involved (During Molecular Dynamic Simulations at any fraction of time)	
		H-bonds	Hydrophobic and pi-pi stacking
TMPRSS2-Camostat mesylate	−54.98 ± 13.31	Asp435, Ser436, Gly439, Ser441, Thr459, Gly462, Gly464	Gln164, Arg165, Lys166, Val275, Val278, His279, Val280, Gly282, His296, Cys297, val298, Glu299, Leu302, Lys342, Asp345, Glu389, Lys390, Lys392, Thr393, Asp345, Aser436, Cys437, Gln438, Gly439, Asp440, Ser441, Gly442, Asp440, Gly 442, Asp458, Thr459, Ser460, Trp461, Gly462, Ser463, Gly464, Ala466, Lys467, Val473, Tyr474
TMPRSS2-Withaferin-A	−37.80 ± 5.80	Lys390, Ser436, Cys437, Ser441, Thr459, Ser460, Trp461, Gly462, Gly464, Tyr474	Ser206, His296, Glu299, Lys342, Glu388, Glu389, Lys390, Gly391, Asp435, Ser436, Cys437, Gln438, Gly439, Asp440, Ser441, Thr459, Ser460, Trp461, Gly464, Lys467, Arg470, Pro471, Val473, Tyr474
TMPRSS2-Withanone	−46.80 ± 5.13	Gln438, Gly439, Asp440, Ser441, Gly462, Ser463, Gly464	His296, Glu299, Lys342, Asp435, Ile381, Ala386, Glu389, Lys390, Val434, Ser436, Cys437, Gln438, Gly439, Asp440, Ser441, Thr459, Ser460, Trp461, Gly462, Ser463, Gly464, Cys465, Ala466, Lys467, Tyr474
TMPRSS2-Withanoside-V	−36.19 ± 7.83	Ala295, His296, Val298, Lys300, Asn303, Ser333, Tyr337, Ser339, Thr341, Lys342, Asn343	Ala259, His296, Val298, Glu299, Lys300, Asn303, Val331, Ile332, Ser333, His334, Pro335, Asn336, Tyr337, Asp338, Ser339, Lys340, Thre341, Lys342, Asn343, Asn344 < asp345, Ile346, Glu389, Cys437, Gln438, Gly439, Asp440, Ser441, Ser460, Trp461, Gly462, ser463, Gly464, Cys465, Lys467, Arg470, Tyr474
TMPRSS2-Withanoside-IV	−42.80 ± 7.46	His296, Ser339, Lys340, Glu389, Asp435, Ser436, Gln438, Ser441, Ser460, Gly462, Gly464, Cys465	VAl280, His296, Glu299, Lys300, Asn336, Tyr337, Asp338, Ser339, Lys340, Thr341, Lys342, Glu338,

Table 2 (*continued*)

Complex	MMGBSA free binding energy (kcal/mol)	Types of interactions and residues involved (During Molecular Dynamic Simulations at any fraction of time)	
		H-bonds	Hydrophobic and pi-pi stacking
			Glu389, Lys390, Val415, Asp417, ASn418, Alu419, Ile420, Thr421, Asp435, Ser436, Cys437, Gln438, Gly439, Asp440, Ser441, Gly442, Asp458, Thr459, Ser460, Trp461, Gly462, Ser463, Gly464, Cys465, Lys467, Arg470
TMPRSS2-Methoxy Withaferin-A	−39.40 ± 3.60	Ser346, Cys437, Ser460, Trp461	His296, Glu299, Tyr337, Lys340, Lys342, Asp345, Ala386, Glu389, Lys390, Gly391, Lys392, tyr416, val434, Ser436, Cys437, Gln438, Gly439, Asp440, Ser441, Thr459, Ser460, Trp461, Gly462, Ser463, Cys465, Lys467, Arg470, Pro471, Val473, Tyr474
TMPRSS2-Withanolide-B	−51.69 ± 7.37	His296, Gly464, Cys465, Ala466	Val280, His296, Cys297, Glu299, Pro301, Leu302, Tyr337, Lys340, Thr341, Lys342, Asp345, Glu389, Lys390, Ser436, Cys437, Gln438, Gly439, Ser441, Trp461, Gly462, Ser463, Gly464, Cys465, Ala466

numerous polar and non-polar interactions with a varying fraction of time at the catalytic site of TMPRSS2. In further analyses, we found that Withanoside-IV had the highest number of consistent interactions (>30% of the simulation time), better than already known inhibitor Camostat mesylate at the catalytic site of TMPRSS2. Only Withanoside-IV, Camostat mesylate and Withanoside-V were found to interact with the catalytic residues (His296, Asp345 and Ser441) for significant duration of simulation time (Fig. 2B-D). Though, Methoxy Withaferin-A and Withanolide-B also had numerous interactions, but no significant bonds were observed with the catalytic domain residues of TMPRSS2 (Fig. 2E and F). On the other hand, Withaferin-A and Withanone interacted most significantly with Ser441 among the important residues (Fig. 2G and H).

MM/GBSA binding energy was then calculated by extracting 100 frames for each protein-ligand complex from the simulated trajectories within the duration of 40 to 100 ns, taking an interval of 30 frames. The average MM/GBSA free binding energy showed that Withanolide-B (−51.69 ± 7.37 kcal/mol), Withanoside-IV (−42.80 ± 7.46 kcal/mol) and Camostat mesylate (−54.98 ± 13.31 kcal/mol) had almost similar binding affinities towards the TMPRSS2, while Withanoside-V (−36.19 ± 7.83 kcal/mol) and Methoxy Withaferin-A (−39.40 ± 3.60 kcal/mol) had little less binding energy, but the values were still comparable with Camostat mesylate. The MM/GBSA binding free energies, as well as all polar and non-polar interactions during the MD simulations are listed in Table 2. These computational analyses thus suggested Withanoside-V
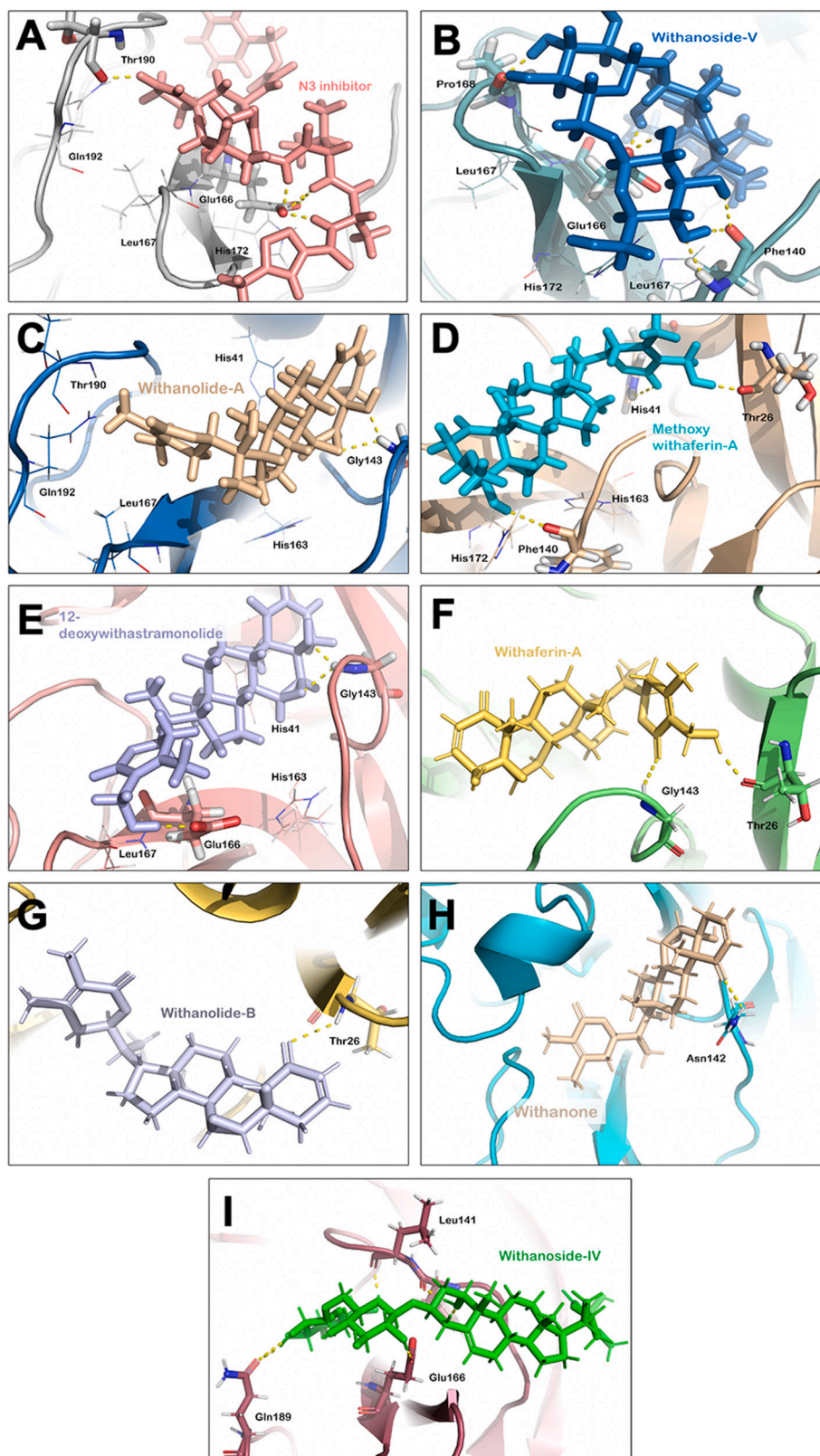
Fig. 3. Interactions of M^pro residues with the ligands in the best docked pose. (A) M^pro-N3 inhibitor (B) M^pro-Withanoside-V (C) M^pro-Withanolide-A (D) M^pro-Methoxy Withaferin-A (E) M^pro-12-deoxywithastramonolide (F) M^pro-Withaferin-A (G) M^pro-Withanolide-B (H) M^pro- Withanone (I) M^pro-Withanoside-IV.

and Withanoside-IV are the best among all the withanolides studied against TMPRSS2 in comparison with Camostat mesylate. In contrast, the interaction of Withanolide-A and 12-deoxywithastramonolide was not stable with TMPRSS2. However, the other withanolides can also be suggested to have the potential to block the interaction between SARS-CoV-2 and TMPRSS2.

Table 3

M^{pro} residues interacting with the ligands in their best docked pose.

Complex	Molecular docking (kcal/mol)	Types of interactions and residues involved (Pre-molecular dynamic simulations)	
		H-bonds	Hydrophobic, polar and pi-pi stacking
M^{pro}-N3 inhibitor	−5.68	Glu166, Thr190	His41, Cys44, Met49, Pro52, Tyr54, Phe140, Leu141, Asn142, His164, Met165, Leu167, Pro168, Thr169, Gly170, His172, Asp187, Arg188, Gln189, Ala191, Gln192
M^{pro}- Withanoside-V	−10.10	Phe140, Glu166, Pro168	His41, Met49, Tyr54, Gly138, Ser139, Leu141, Asn142, Gly143, Ser144, Cys145, His163, His164, Met165, Leu167, Thr169, Gly170, His172, Asp187, Arg188, Gln189
M^{pro}- Withanoside-IV	−6.39	Phe140, Leu141, Cys145, Glu166, Gln189	Lys5, His41, Gln127, Tyr126, Lys137, Gly138, Ser139, Asn142, Gly143, Ser144, His163, His164, Met165, Gly170, Val171, His172, Glu290
M^{pro}-Methoxy Withaferin-A	−4.24	Thr26, His41, Phe140	Thr25, Leu27, Met49, Leu141, Asn142, Gly143, Ser144, Cys145, His163, His164, Met165, Glu166, His172, Gln189
M^{pro}- Withanolide-B	−3.36	Thr26	Thr24, Thr25, His41, Ser46, Met49, Tyr54, Asn142, Gly143, Ser144, Cys145, His164, Met165, Glu166, Asp187, Arg188, Gln189
M^{pro}- Withanolide-A	−4.15	Gly143	Thr25, Thr26, Leu27, His41, Met49, Leu141, Asn142, Ser144, Cys145, His163, Met165, Glu166, Leu167, Pro168, Arg188, Gln189, Thr190, Ala191, Gln192
M^{pro}-12-deoxywithastramonolide	−3.36	Gly143, Glu166	Thr25, Thr26, Leu27, His41, Met49, Leu141, Asn142, Ser144, Cys145, His163, His164, Met165, Leu167, Pro168, Gly170, Gln189
M^{pro}-Withaferin-A	−3.75	Thr26, Gly143	Thr25, Leu27, His41, Met49, Phe140, Leu141, Asn142, Ser144, Cys145, His163, His164, Met165, Glu166, His172, Gln189
M^{pro}-Withanone	−4.42	Asn142	Thr 24, Thr 25, Thr26, Leu27His41, Met49, Tyr54, Gly 143, Cys145, His164, Met165, Glu166, Arg188, Gln189

3.2. Binding affinity of withanolides towards SARS-CoV-2 Main protease (M^{pro}) predicted Withanoside-V as the best among all the withanolides

N3, a synthetic peptidomimetic compound has been reported to target the substrate binding pocket of the main protease across different variants of coronavirus including SARS-CoV-2 [30,56]. We first estimated the docking score for the N3 inhibitor bound to M^{pro} at the same site as in PDB 6LU7, which was found to be −5.68 kcal/mol. The N3 inhibitor was making hydrogen bonds with Glu166 and Thr190 of M^{pro}. Among all the withanolides, Withanoside-V docked with M^{pro} with a score of −10.10 kcal/mol, which was almost double the docking score for the N3 inhibitor. The docking score for other withanolides was also comparable to that of N3 inhibitor. The best-docked pose for all the M^{pro}-ligand complexes showing the hydrogen bonded interactions is illustrated in Fig. 3, while all the polar and non-polar interactions of best-docked pose along with docking scores, has been summarized in Table 3. In order to further look into the binding affinity and the stability of the docked ligands, we subjected each of the protein-withanolide complex to MD simulations. The interactions of Withanoside-IV, Withaferin-A and Withanolide-B were not strong enough and the ligands came out of the binding pocket of M^{pro} within 30–40 ns of the simulation run. While the other withanolides - Withanone, Withanoside-V, Withanolide-A, Methoxy Withaferin-A and 12-deoxywithastramonolide interacted stably with the protein throughout the course of simulation. The inhibitory potential of Withanone against M^{pro} has been shown in one of our previous reports as well [16]. No significant fluctuations were observed in the RMSD of these ligands just after 10 ns of simulation time (Supplementary Fig. 3A). All the interacting M^{pro}-ligand complexes got stable within 10 ns of the simulation (Supplementary Fig. 3B). The RMSF plot showed that all the complexes along with the Apo form of M^{pro} had similar flexibility/fluctuation of amino acid residues, and overall, these fluctuations were less than 2.5 Å in each of the system (Supplementary Fig. 3C). Next, we investigated the hydrogen bonding pattern for all these complexes. We found that N3 inhibitor was forming the highest number of the hydrogen bonds (4.9 ± 1.1) with M^{pro}, followed by Withanoside-V (2.16 ± 1.4), 12-deoxywithastramonolide (1.3 ± 1.01), Methoxy Withaferin-A (0.89 ± 0.65) and Withanolide-A (0.43 ± 0.57) (Fig. 4A). Further various properties of the ligands were calculated and assessed, and it was found that all the withanolides had similar stability bound with M^{pro}. All the properties of the complexes, as well as ligands alone, are given in Supplementary Table 2. To further explore the crucial catalytic site residues of M^{pro}, which were involved in significant interactions (more than 30% of the simulation time) with withanolides, simulation interaction occupancy was calculated. It was found that in

M^{pro}-N3 inhibitor complex, Asn142, Glu166 and Thr190 were mainly involved in the significant interactions. Interestingly, all the ligands had various polar and non-polar interactions at the catalytic site of M^{pro}, but Glu166, Cys145 and Gln192 were found to be the crucial residues which were forming significant interactions with the ligands and providing them stability (Fig. 4B-G). Finally, to investigate the binding affinity of the ligands towards M^{pro}, the MM/GBSA free binding energy was calculated using 100 frames spanned over 40 to 100 ns for each of the protein-ligand complex. N3 was estimated to have the highest free binding energy of -64.10 ± 10 kcal/mol, followed by Withanoside-V (-35.69 ± 5.17 kcal/mol), Withanolide-A (-30.19 ± 7.27 kcal/mol), 12-deoxywithastramonolide (-28.09 ± 6.77 kcal/mol) and Methoxy Withaferin-A (-27.84 ± 3.15 kcal/mol). All the interactions and MM/GBSA free binding energy for each of the M^{pro}-withanolide complex are given in Table 4. This data thus suggests the potential of these withanolides as possible inhibitors of the main protease of SARS-CoV-2.

3.3. Withanolides caused downregulation of TMPRSS2 expression in host cells

Next, we performed cell-based TMPRSS2 expression screening for the withanolides. We first examined the levels of TMPRSS2 expression in various cancer cell lines (Supplementary Fig. 4A) and selected four *i.e.*, T.Tn, HSC3, A549 and MCF7 possessing low to moderate levels of TMPRSS2 expression. T.Tn cells were used for the initial screening of the withanolides by reverse transcription PCR (RT-PCR) using TMPRSS2-specific primers. Cells were treated with non-toxic doses of withanolides. As shown in Fig. 5A, Withaferin-A, Withanone, Withanoside-IV and Withanoside-V treated cells showed remarkable decrease in the level of TMPRSS2 mRNA. Triethylene glycol that is also found in Ashwagandha leaves did not show any effect. Taken together, these data suggested that, in addition to Withanone reported earlier [16], Withaferin-A, Methoxy Withaferin-A, Withanolide-A, Withanolide-B, Withanoside-IV and Withanoside-V could cause downregulation of TMRPSS2 expression and therefore may be useful for COVID-19 management. Furthermore, Withanolide-A and 12-deoxywithastramonolide although did not show stable interaction with TMPRSS2 in molecular docking analyses, caused a significant decrease in the TMPRSS2 mRNA suggesting multiple inhibitory mechanism of these withanolides.

Based on the above data, we shortlisted Withaferin-A, Withanone, Withanolide-A, Withanoside-IV and Withanoside-V and investigated their effects on TMPRSS2 mRNA and protein in additional cell lines. Supplementary Fig. 5A shows the MTT assay with the non-toxic doses of withanolides, where no significant decrease in cell viability was

Fig. 4. The comparison of number of hydrogen bond counts throughout the simulations for different M^{pro}-ligand complexes (A). The occupancy of M^{pro} residues while making polar and non-polar interactions with N3 inhibitor and different withanolides as observed over the entire simulation trajectory. (B) M^{pro}-N3 inhibitor (C) M^{pro}-Withanoside-V (D) M^{pro}-Methoxy Withaferin-A (E) M^{pro}-Withanolide-A (F) M^{pro}-12-deoxywithastramonolide (G) M^{pro}-Withanone.

Table 4

Residues of M^pro interacting with the ligands during the course of MD simulations along with the free binding energy of each protein-ligand complex.

Complex	MMGBSA free binding energy (kcal/mol)	Types of interactions and residues involved (During Molecular Dynamic Simulations at any fraction of time)	
		H-bonds	Hydrophobic and pi-pi stacking
M^pro- N3 inhibitor	−64.05 ± 10.17	Asn142,Glu166, Arg188, Gln189, Thr190, Gln192	Thr25, His41, Ser46, Met49, Lys137, Gly138, Phe140, Leu141, Asn142, Gly143, Cys145, His163, His164, Met165, Glu166, Leu167, Pro168, Thr169, Gly170, His172, Val186, Arg188,Gln189, Thr190, Ala191, Gln192, Ala193
M^pro- Withanoside-V	−35.70 ± 5.17	Phe140, Asn142, Glu166, Pro168, Thr169, Arg188, Gln189, Thr190, Gln192, Arg222	Thr25, His41, Ser46, Met49, Lys137, Gly138, Ser139, Phe140, Leu141, Asn142, Ser144, Cys145, Met165, Glu166, Leu167, pro168, Thr169, Gly170, His172, Val186, Asp187,Arg188, Gln189, Thr190, Ala191, Gln192, Ala193, Ala194, Gly195, Thr196, Arg217, Leu220, Asn221, Arg222, Phe223, Thr224, Glu270
M^pro- Methoxy Withaferin-A	−27.84 ± 3.15	His41, Glu166, Gln189, Thr190	Thr24, Thr25, Thr26, Leu27, His41, Cys44, Thr45, Ser46, Glu57, Met49, Leu50, Asn51, Ser139, Phe140, Asn142, Gly143, Cys145, Met165, Glu166, Leu167, Pro168, Thr169, Gly170, Val186, Asp187, Arg188, Gln189, Thr190, Ala191, Gln192
M^pro-12-deoxywithastramonolide	−30.19 ± 7.27	Thr25, Asn142, Gly143, Glu166, Gln189, Gln192	Thr24, Thr25, Thr26, Leu27, His41, Cys44, Thr45, Ser46, Met49, Asn142, Gly143, Ser144, Cys145, His163, Met165, Glu166, Leu167, Pro168, Thr169, Phe185, Gln189, Thr190, Ala191, Gln192, Ala193
M^pro-Withanone	−28.07 ± 6.77	Thr26, Ser46, Asn142, Gly143, Glu166, Gln189	Gln19, Thr21, Gly23, Thr24, Thr25, Thr26, Leu27, Asn28, His41, Val42, Cys44, Ser46, Glu47, Met49, Asn119, Gly120, Phe140, leu141, Asn142, Gly143, Ser144, Cys145, Met165, Glu166, Leu167, Pro168, Val186, Asp187, Arg188, Gln189, Thr190, Gln192

observed upon treatment, in comparison to the untreated control group. Short-term and long-term cell viability assays were also performed to determine the non-toxic doses for each cell line using QCV assay as reported earlier [57]. As shown in Supplementary Figs. 5B and 5C, no significant difference was observed in cell number or colony forming ability of the T.Tn cells when compared to the untreated control group. Next, we treated HSC3 cells with non-toxic doses of Withaferin-A, Withanone, Withanolide-A, Withanoside-IV and Withanoside-V, and investigated TMPRSS2 mRNA. As shown in Fig. 5B and similar to T.Tn cells, all the compounds (used at their non-toxic doses, determined by independent experiments) caused a significant reduction in TMPRSS2 mRNA in HSC3 cells. To further validate the above data, the protein level of TMPRSS2 was determined in control and treated cells by Western blotting. Treatment with Withaferin-A, Withanone, Withanoside-IV and Withanoside-V was found to downregulate TMPRSS2 protein; maximum reduction was observed in cells treated with Withanone (Fig. 5C). Consistent with the Western blotting results, we observed decrease in TMPRSS2 protein in treated cells by immuno-staining (Fig. 5D). The expression of TMPRSS2 has been reported to vary among different tissues/organs [58,59]. To account for this variation and to examine that the effect of withanolides is not dependent on cell lines used, we performed the same analyses in two more cell lines *i.e.*, A549 and MCF7. All the five withanolides - Withaferin-A, Withanone, Withanolide-A, Withanoside-IV and Withanoside-V, caused decrease in the mRNA levels of TMPRSS2 in both the cell lines. TMPRSS2 protein was also found to be less in the treated cells in comparison to the control group (Supplementary Fig. 6).

3.4. Selected withanolides caused inhibition of SARS-CoV-2 replication

We then tested the different withanolides for their ability to inhibit SARS-CoV-2 replication in Vero E6 cells. As shown in Table 5, several withanolides caused downregulation of expression of viral envelope (*E*-gene) and nucleocapsid sequences (*N*-gene) (as determined by Real-time PCR) signifying their potential to inhibit virus replication. A known anti-virus drug, Remdesivir, was used as a positive control. It caused dose-dependent decrease in virus replication as determined by RT-PCR of E-gene (Supplementary Fig. 4B). Remdesivir-treated cells showed 68% and 75% inhibition of virus replication based on the of E-gene and N-gene expression at 24 h post-infection, respectively. At 48 h post-infection, Remdesivir (10 mM) caused 99% inhibition of virus replication. Methoxy Withaferin-A caused the least effect (17%; average inhibition of E-gene and N-gene expression) among all withanolides tested. Withanolide-A, Withanoside-IV and 12-deoxywithastramonolide caused

<50% inhibition of E-gene and N-gene. On the other hand, Withanone, Withanolide-B and Withanoside-V treated cells showed average of ~66%, 84% and 73% inhibition of E-gene and N-gene expression, respectively at 48 h post-infection (Table 5). Dose-response analysis revealed 35–99% reduction of virus titer in the range of 0.01 to 10 mM Remdesivir-treated cells even at 24 h incubation. On the other hand, withanolides did not show effect at doses lower than 10 mM.

3.5. Water-based Ashwagandha leaf extracts caused decrease in TMPRSS2

Based on the above data showing that cells treated with different withanolides showed significant downregulation of TMPRSS2, and most of these withanolides showed potential to block activitiy of TMPRSS2 and M^pro, we predicted that the extracts enriched in withanolides may provide an easy and economic source to block entry of corona virus to host cells as well as inhibit its replication. We have earlier optimized the extraction of two of the major withanolides- Withaferin-A and With-anone using cyclodextrin [60]. As reported earlier, leaves possess highest content of withanolides; whereas stem possesses a relatively high ratio of Withanone to Withaferin-A [60–61]. We prepared leaf and stem extracts [60], and investigated the content of 8 withanolides. As shown in Fig. 5E, along with Withaferin A and Withanone, we detected Withanolide IV, Withanolide V and 12-deoxywithastramonolide in water soluble and insoluble extracts of leaves. 12-deoxywithastramono-lide was also detected in stem extracts. We next examined TMPRSS2 expression in the extract (non-toxic concentration, as determined by short and long term MTT assays; Supplementary Fig. 5)-treated cells. As shown in Fig. 5F-H, the extracts caused downregulation of TMPRSS2 expression at both transcriptional (Fig. 5F) and translational levels (Fig. 5G and H), thereby suggesting the possible use of extracts as an effective alternative to the pure Ashwagandha-derived compounds.

4. Discussion

COVID-19 pandemic has triggered research on the anti-viral activity of various kinds of natural products. In traditional home medicine systems, herbs and other natural products are commonly used to enhance immunity, strengthen physical and metal health, as well as prevent and treat various diseseaes. Given that the herbs offer widely available, easy and economic resource, numerous research groups began to investigate anti-SARS-CoV-2 potential of herbal component including flavonoids, steroids, phenols and withanolides [62–65]. Most of these studies have tested the efficacy of the test compounds to target either the SARS-CoV-2
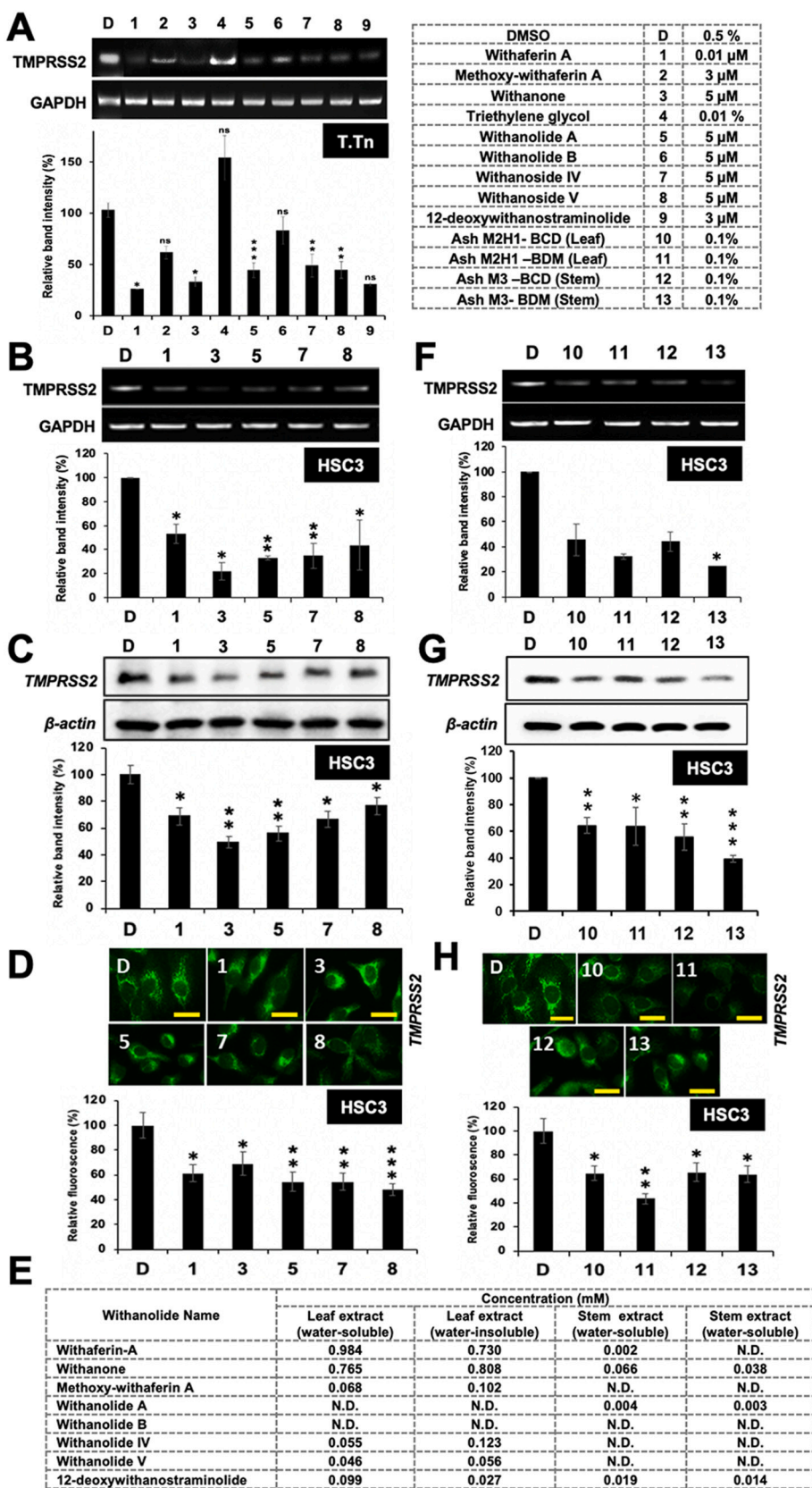
Fig. 5. Effect of different withanolides on TMPRSS2 mRNA levels in T.Tn cells (A). Effect of Withaferin-A, Withanone, Withanolide-A, Withanoside-IV and Withanoside-V, in particular, on TMPRSS2 in HSC3 cells. Downregulation of TMPRSS2 mRNA was observed (B), TMPRSS2 protein was also found to be decreased due to the treatment with withanolides as seen using western blots and immunostaining (C and D). Withanolide content in Ashwagandha leaf and stem extracts (E) and downregulation of TMPRSS2 mRNA (F) and protein (G and H) in cells treated with extracts.

Table 5

Inhibition of SARS-CoV-2 replication by withanolides.

Compound (10 μM)	Percent cell viability		Percent inhibition				
			24 h			48 h	
	24 h	48 h	E	N		E	N
Methoxy Withaferin A	95.15	85.7	0	13.47		8.78	25.78
Withanone	96.09	90.43	20.73	24		65.93	66.52
Withanolide A	87.8	74.76	0	15.38		21.38	35.09
Withanolide B	96.17	78.12	7.18	28.14		86.25	82.18
Withanoside IV	89.85	77.35	16.28	37.77		45.03	44.79
Withanoside V	94.35	78.68	18.55	39.65		74.9	72.99
12-deoxywithastramonolide	89.18	76	17.35	37.14		54.75	35.09
Remdesivir	99.23	94.37	68.84	75.63		99.76	99.78

Percent inhibition of virus replication based on the Ct values for the detection of envelope (E) and nucleocapsid (N) gene sequences is shown at 24 and 48 h post-infection.

proteins or host cell surface proteins (ACE-2 and TMPRSS2) by *in-silico* analysis such as virtual screening, molecular docking and MD simulations [44,66,67]. In this study, we have carried out extensive computational, experimental as well as anti-viral assays to emphasize on the anti-SARS-CoV-2 activities of major withanolides and withanolides enriched Ashwagandha extracts.

The computational analysis carried out to study the interaction of different withanolides with TMPRSS2 and M^{pro} predicted Withanoside-IV and Withanoside-V to be the top scoring compounds after docking. The binding of Withanoside-V to both the molecular targets was remarkably stable when the docked complexes were subjected to 100 ns MD simulation. Although Withanoside-IV interacted well with TMPRSS2, it could not stay within the binding pocket of M^{pro} subsequent to MD simulations. In line with these predictions, we observed ~70% decrease in the viral replication in cells treated with Withanoside-V, whereas Withanoside-IV showed inhibition of viral activity by ~40%. Moreover, despite a comparative low docking score, the MM/GBSA binding free energy of Withanolide-B with TMPRSS2 was found to be the highest, which corresponded well in the antiviral activity assay also. The MM/GBSA binding free energy is generally used for predicting the binding affinity of the candidate ligands with respect to each other against a specific target. Further, the most substantial inhibition of the viral activity (~80%) was obtained with the treatment of cells with Withanolide-B. Next, Withanone was consistently predicted to be a potential candidate with inhibitory activity against both TMPRSS2 and M^{pro}. It could also cause the transcriptional downregulation of the expression of TMPRSS2, as shown in Fig. 5A and B, and had also been reported in our previous study [44]. TMPRSS2 is enriched in cancer cells (especially in case of pancreatic cancer) and has been considered as a anti-cancer drug target [5,8,48,50,51]. The downregulation of TMPRSS2 in Withanolide-treated cells may also account for anti-cancer potential of Withanolides. Withanone has earlier been shown to cause activation of tumor suppressor pathways and inhibit cancer cell proliferation [36–43] some of which may also account for its anti-viral activity. It also interacted with M^{pro} with a docking score of −4.42 kcal/mol, and possessed good binding affinity (−28.07 ± 6.77 kcal/mol) towards the M^{pro} enzyme as indicated by the MM/GBSA binding free energy analysis. The effect of Withanone on SARS-CoV-2 was further supported by the antiviral activity assay, where a drop of 45–60% was recorded in viral *E*-gene and N-gene expressions signifying inhibition of virus replication in several independent experimentsAmong all the tested withanolides, Methoxy Withaferin-A was the weakest candidate with low interaction energies. In line with the computational data, only ~17% inhibition in viral replication was observed in the SARS-CoV-2 antiviral assay. It also did not cause significant downregulation of TMPRSS2 mRNA in RT-PCR screening. Similar to this, 12-deoxywithastramonolide was not selected in RT-PCR assay. The computational assay showed that it can interact with M^{pro}, but not TMPRSS2. Very much in line with these data, its effect on virus replication was weak (<50%).

Furthermore, Withanolide-A was the only withanolide that did not interact stably with any of the two molecular targets as observed during the MD simulations. However, it caused significant downregulation of TMPRSS2 mRNA (Fig. 5A and B) that could be attributed to only ~28% inhibition of viral infection in Withanolide-A treated cells. Dose response (0.01 to 10 mM) experiments showed that while Remdesivir caused 35–99% inhibition of virus replication in Vero E6 cells, most withanolides neither showed any effect at doses lower than 10 mM, nor any clear dose response. We anticipated that such effect may be due to the stability issues of the purified compounds and therefore recruited crude extracts from Ashwagandha leaves and stems that provided natural mixture of a variety of withanolides. As shown in Fig. 5 and Supplementary Fig. 6, human cells treated with non-toxic doses of these extracts showed inhibition of TMPRSS2 expression both at the mRNA and protein levels. In anti-viral assays, SARS-CoV-2 infected Vero E6 cells treated with non-toxic doses (0.001, 0.005 and 0.01%) of leaf extract showed a dose-dependent downregulation (38%, 44% and 90%, respectively) of viral E gene signifying inhibition of viral replication in extract-treated cells. Of note, although most of the withanolides have been shown to be non-toxic (Withaferin-A and Withanone are the only two that have been shown to be cytotoxic in *in vitro* and *in vivo* studies using human cancer cells and mice models), extensive dose response analyses on the anti-viral activity of high doses of withanolides are warranted. Collectively, computational and *in vitro* analyses highlighted the multi-mode mechanism of action of different withanolides. Interestingly, the water-based Ashwagandha extracts containing a natural mixture of withanolides also caused a significant reduction of TMPRSS2 mRNA in treated cells, and thus is proposed as a candidate resource for COVID-19 treatment, warranting further laboratory and clinical studies.

5. Conclusion

The grave consequences of the COVID-19 pandemic have brought an urgent need for rapid search of effective therapy against SARS-CoV-2. Repurposing of the existing drugs in last few months has promoted some molecules to clinical testing. We have earlier reported the potential of Ashwagandha withanolides (Withaferin-A and Withanone) to inhibit host cell receptor TMPRSS2 and the main protease of SARS-CoV-2. By extensive computational and experimental analyses on nine withanolides, we report that most of these can downregulate TMPRSS2 and some, including Withanoside-V, Withanone and Methoxy Withaferin-A possess the ability to inhibit the activity of both TMPRSS2 and M^{pro}. Importantly, some of the withanolides caused inhibition of SARS-CoV-2 replication in the cell culture. These data warrant further validation at the experimental and clinical levels. Due to the fact that pure compounds are often expensive and not widely available, we prepared Ashwagandha extracts enriched with withanolides that may be useful resource for COVID-19 treatment.

CRediT authorship contribution statement

J.K.D. contributed to computational analysis, experimental validation and manuscript writing; V.K. contributed to computational analysis and manuscript writing; S.G. contributed to experimental validation and manuscript writing; C.S. contributed to experimental validation; S.A. contributed to experimental validation; R.S.K. contributed to experimental validation; J.W. contributed to experimental validation; H.Z. contributed to experimental validation; A.K contributed to experimental validation; S.C.K. contributed to conception and manuscript writing; S. V. contributed to conception, manuscript writing and funding; D.S. contributed to conception, design, manuscript writing and funding; R. W. contributed to conception, design, manuscript writing and funding.

Declaration of competing interest

The authors declare no conflict of interest.

Data availability

Source data for all the figures are provided with the paper.

Appendix A. Supplementary data

Supplementary data to this article can be found online at https://doi.org/10.1016/j.ijbiomac.2021.06.015.

References

[1] WHO, WHO Coronavirus Disease (COVID-19) dashboard (2020), Data last updated: 2020/10/16. Retrieved from, https://covid19.who.int, 2020.

[2] S.J. Anthony, C.K. Johnson, D.J. Greig, S. Kramer, X. Che, H. Wells, A.L. Hicks, D.O. Joly, N.D. Wolfe, P. Daszak, W. Karesh, W.I. Lipkin, S.S. Morse, P. Consortium, J.A.K. Mazet, T. Goldstein, Global patterns in coronavirus diversity, Virus Evol. 3 (1) (2017), vex012.

[3] S. Su, G. Wong, W. Shi, J. Liu, A.C.K. Lai, J. Zhou, W. Liu, Y. Bi, G.F. Gao, Epidemiology, genetic recombination, and pathogenesis of coronaviruses, Trends Microbiol. 24 (6) (2016) 490–502.

[4] M.A. Tortorici, D. Veesler, Structural insights into coronavirus entry, Adv. Virus Res. 105 (2019) 93–116.

[5] e8 M. Hoffmann, H. Kleine-Weber, S. Schroeder, N. Kruger, T. Herrler, S. Erichsen, T.S. Schiergens, G. Herrler, N.H. Wu, A. Nitsche, M.A. Muller, C. Drosten, S. Pohlmann, SARS-CoV-2 cell entry depends on ACE2 and TMPRSS2 and is blocked by a clinically proven protease inhibitor, Cell 181 (2) (2020) 271–280.

[6] N. Iwata-Yoshikawa, T. Okamura, Y. Shimizu, H. Hasegawa, M. Takeda, N. Nagata, TMPRSS2 contributes to virus spread and immunopathology in the airways of murine models after coronavirus infection, J. Virol. 93 (6) (2019) e01815–18.

[7] S. Matsuyama, N. Nao, K. Shirato, M. Kawase, S. Saito, I. Takayama, N. Nagata, T. Sekizuka, H. Katoh, F. Kato, M. Sakata, M. Tahara, S. Kutsuna, N. Ohmagari, M. Kuroda, T. Suzuki, T. Kageyama, M. Takeda, Enhanced isolation of SARS-CoV-2 by TMPRSS2-expressing cells, Proc. Natl. Acad. Sci. U. S. A. 117 (13) (2020) 7001–7003.

[8] T.S. Kim, C. Heinlein, R.C. Hackman, P.S. Nelson, Phenotypic analysis of mice lacking the Tmprss2-encoded protease, Mol. Cell. Biol. 26 (3) (2006) 965–975.

[9] L.W. Shen, H.J. Mao, Y.L. Wu, Y. Tanaka, W. Zhang, TMPRSS2: a potential target for treatment of influenza virus and coronavirus infections, Biochimie 142 (2017) 1–10.

[10] E. Bottcher, C. Freuer, T. Steinmetzer, H.D. Klenk, W. Garten, MDCK cells that express proteases TMPRSS2 and HAT provide a cell system to propagate influenza viruses in the absence of trypsin and to study cleavage of HA and its inhibition, Vaccine 27 (45) (2009) 6324–6329.

[11] P. Zhou, X.L. Yang, X.G. Wang, B. Hu, L. Zhang, W. Zhang, H.R. Si, Y. Zhu, B. Li, C.L. Huang, H.D. Chen, J. Chen, Y. Luo, H. Guo, R.D. Jiang, M.Q. Liu, Y. Chen, X.R. Shen, X. Wang, X.S. Zheng, K. Zhao, Q.J. Chen, F. Deng, L.L. Liu, B. Yan, F.X. Zhan, Y.Y. Wang, G.F. Xiao, Z.L. Shi, A pneumonia outbreak associated with a new coronavirus of probable bat origin, Nature 579 (7798) (2020) 270–273.

[12] F. Wu, S. Zhao, B. Yu, Y.M. Chen, W. Wang, Z.G. Song, Y. Hu, Z.W. Tao, J.H. Tian, Y.Y. Pei, M.L. Yuan, Y.L. Zhang, F.H. Dai, Y. Liu, Q.M. Wang, J.J. Zheng, L. Xu, E. C. Holmes, Y.Z. Zhang, A new coronavirus associated with human respiratory disease in China, Nature 579 (7798) (2020) 265–269.

[13] A. Hegyi, J. Ziebuhr, Conservation of substrate specificities among coronavirus main proteases, J. Gen. Virol. 83 (Pt 3) (2002) 595–599.

[14] T. Pillaiyar, M. Manickam, V. Namasivayam, Y. Hayashi, S.H. Jung, An overview of severe acute respiratory syndrome-coronavirus (SARS-CoV) 3CL protease inhibitors: peptidomimetics and small molecule chemotherapy, J. Med. Chem. 59 (14) (2016) 6595–6628.

[15] P.C. Woo, Y. Huang, S.K. Lau, K.Y. Yuen, Coronavirus genomics and bioinformatics analysis, Viruses 2 (8) (2010) 1804–1820.

[16] V. Kumar, J.K. Dhanjal, S.C. Kaul, R. Wadhwa, D. Sundar, Withanone and caffeic acid phenethyl ester are predicted to interact with main protease (M(pro)) of SARS-CoV-2 and inhibit its activity, J. Biomol. Struct. Dyn. (2020) 1–13.

[17] E. Bottcher-Friebertshauser, D.A. Stein, H.D. Klenk, W. Garten, Inhibition of influenza virus infection in human airway cell cultures by an antisense peptide-conjugated morpholino oligomer targeting the hemagglutinin-activating protease TMPRSS2, J. Virol. 85 (4) (2011) 1554–1562.

[18] E. Bottcher-Friebertshauser, Y. Lu, D. Meyer, F. Sielaff, T. Steinmetzer, H.D. Klenk, W. Garten, Hemagglutinin activating host cell proteases provide promising drug targets for the treatment of influenza a and B virus infections, Vaccine 30 (51) (2012) 7374–7380.

[19] E. Bottcher-Friebertshauser, H.D. Klenk, W. Garten, Activation of influenza viruses by proteases from host cells and bacteria in the human airway epithelium, Pathog. Dis. 69 (2) (2013) 87–100.

[20] M. Ohkoshi, T. Oka 12 (1984) 148–152.

[21] S. Ikeda, M. Manabe, T. Muramatsu, K. Takarnori, H. Ogawa, Protease inhibitor therapy for recessive dystrophic epidermolysis bullosa: in vitro effect and clinical trial with camostat mesylate, J. Amer. Acad. Dermatolol. 18 (6) (1988) 1246–1252.

[22] B. Göke, F. Stöckmann, R. Müller, P. Lankisch, W. Creutzfeldt, Effect of a specific serine protease inhibitor on the rat pancreas: systemic administration of camostate and exocrine pancreatic secretion, Digestion 30 (3) (1984) 171–178.

[23] G. Adler, A. Müllenhoff, I. Koop, T. Bozkurt, B. Göke, C. Beglinger, R. Arnold, Stimulation of pancreatic secretion in man by a protease inhibitor (camostate), Eur. J. Clin. Investig. 18 (1) (1988) 98–104.

[24] J.K. Sai, M. Suyama, Y. Kubokawa, Y. Matsumura, K. Inami, S. Watanabe, Efficacy of camostat mesilate against dyspepsia associated with non-alcoholic mild pancreatic disease, J. Gastroenterol. 45 (3) (2010) 335–341.

[25] J.Nuttall M.L. Ramsey P.A. Hart, A phase 1/2 trial to evaluate the pharmacokinetics, safety, and efficacy of NI-03 in patients with chronic pancreatitis: study protocol for a randomized controlled trial on the assessment of camostat treatment in chronic pancreatitis (TACTIC), Trials 20 (1) (2019) 501.

[26] M. Kawase, K. Shirato, L. van der Hoek, F. Taguchi, S. Matsuyama, Simultaneous treatment of human bronchial epithelial cells with serine and cysteine protease inhibitors prevents severe acute respiratory syndrome coronavirus entry, J. Virol. 86 (12) (2012) 6537–6545.

[27] K. Shirato, M. Kawase, S. Matsuyama, Middle East respiratory syndrome coronavirus infection mediated by the transmembrane serine protease TMPRSS2, J. Virol. 87 (23) (2013) 12552–12561.

[28] W. Dai, B. Zhang, X.M. Jiang, H. Su, J. Li, Y. Zhao, X. Xie, Z. Jin, J. Peng, F. Liu, C. Li, Y. Li, F. Bai, H. Wang, X. Cheng, X. Cen, S. Hu, X. Yang, J. Wang, X. Liu, G. Xiao, H. Jiang, Z. Rao, L.K. Zhang, Y. Xu, H. Yang, H. Liu, Structure-based design of antiviral drug candidates targeting the SARS-CoV-2 main protease, Science 368 (6497) (2020) 1331–1335.

[29] L. Zhang, D. Lin, X. Sun, U. Curth, C. Drosten, L. Sauerhering, S. Becker, K. Rox, R. Hilgenfeld, Crystal structure of SARS-CoV-2 main protease provides a basis for design of improved alpha-ketoamide inhibitors, Science 368 (6489) (2020) 409–412.

[30] Z. Jin, X. Du, Y. Xu, Y. Deng, M. Liu, Y. Zhao, B. Zhang, X. Li, L. Zhang, C. Peng, Y. Duan, J. Yu, L. Wang, K. Yang, F. Liu, R. Jiang, X. Yang, T. You, X. Liu, X. Yang, F. Bai, H. Liu, X. Liu, L.W. Guddat, W. Xu, G. Xiao, C. Qin, Z. Shi, H. Jiang, Z. Rao, H. Yang, Structure of M(pro) from SARS-CoV-2 and discovery of its inhibitors, Nature 582 (7811) (2020) 289–293.

[31] B. Cao, Y. Wang, D. Wen, W. Liu, J. Wang, G. Fan, L. Ruan, B. Song, Y. Cai, M. Wei, X. Li, J. Xia, N. Chen, J. Xiang, T. Yu, T. Bai, X. Xie, L. Zhang, C. Li, Y. Yuan, H. Chen, H. Li, H. Huang, S. Tu, F. Gong, Y. Liu, Y. Wei, C. Dong, F. Zhou, X. Gu, J. Xu, Z. Liu, Y. Zhang, H. Li, L. Shang, K. Wang, K. Li, X. Zhou, X. Dong, Z. Qu, S. Lu, X. Hu, S. Ruan, S. Luo, J. Wu, L. Peng, F. Cheng, L. Pan, J. Zou, C. Jia, J. Wang, X. Liu, S. Wang, X. Wu, Q. Ge, J. He, H. Zhan, F. Qiu, L. Guo, C. Huang, T. Jaki, F.G. Hayden, P.W. Horby, D. Zhang, C. Wang, A Trial of Lopinavir-Ritonavir in adults Hospitalized with Severe Covid-19, N. Engl. J. Med. 382 (19) (2020) 1787–1799.

[32] B. Nutho, P. Mahalapbutr, K. Hengphasatporn, N.C. Pattaranggoon, N. Simanon, Y. Shigeta, S. Hannongbua, T. Rungrotmongkol, Why are lopinavir and ritonavir effective against the newly emerged coronavirus 2019? Atomistic insights into the inhibitory mechanisms, Biochemist 59 (18) (2020) 1769–1779.

[33] T. Shi, E. Wilhelm, B. Bell, N. Dumais, Nf-?b-Dependent inhibition of HIV-1 transcription by withaferin A, HIV, Curr. Res. 2 (119) (2017), 2572-0805.1000119.

[34] Suppl A. Grover, V. Agrawal, A. Shandilya, V.S. Bisaria, D. Sundar, Non-nucleosidic inhibition of Herpes simplex virus DNA polymerase: mechanistic insights into the anti-herpetic mode of action of herbal drug withaferin a, BMC Bioinf. 12 (Suppl 13) (2011) 13:S22.

[35] Z. Cai, G. Zhang, B. Tang, Y. Liu, X. Fu, X. Zhang, Promising anti-influenza properties of active constituent of Withania somnifera ayurvedic herb in targeting neuraminidase of H1N1 influenza: computational study, Cell Biochem. Biophys. 72 (3) (2015) 727–739.

[36] A. Grover, R. Singh, A. Shandilya, D. Priyandoko, V. Agrawal, V.S. Bisaria, R. Wadhwa, S.C. Kaul, D. Sundar, Ashwagandha derived withanone targets TPX2-Aurora a complex: computational and experimental evidence to its anticancer activity, PLoS One 7 (1) (2012), e30890.

[37] A. Grover, D. Priyandoko, R. Gao, A. Shandilya, N. Widodo, V.S. Bisaria, S.C. Kaul, R. Wadhwa, D. Sundar, Withanone binds to mortalin and abrogates mortalin-p53 complex: computational and experimental evidence, Int. J. Biochem. Cell Biol. 44 (3) (2012) 496–504.

[38] N. Widodo, K. Kaur, B.G. Shrestha, Y. Takagi, T. Ishii, R. Wadhwa, S.C. Kaul, Selective killing of cancer cells by leaf extract of Ashwagandha: identification of a tumor-inhibitory factor and the first molecular insights to its effect, Clin. Cancer Res. 13 (7) (2007) 2298–2306.

[39] Y. Yu, S.P. Katiyar, D. Sundar, Z. Kaul, E. Miyako, Z. Zhang, S.C. Kaul, R.R. Reddel, R. Wadhwa, Withaferin-A kills cancer cells with and without telomerase: chemical, computational and experimental evidences, Cell Death Dis. 8 (4) (2017), e2755.

[40] D. Sundar, Y. Yu, S.P. Katiyar, J.F. Putri, J.K. Dhanjal, J. Wang, A.N. Sari, E. Kolettas, S.C. Kaul, R. Wadhwa, Wild type p53 function in p53(Y220C) mutant harboring cells by treatment with Ashwagandha derived anticancer withanolides: bioinformatics and experimental evidence, J. Exp. Clin. Cancer Res. 38 (1) (2019) 103.

[41] N. Widodo, D. Priyandoko, N. Shah, R. Wadhwa, S.C. Kaul, Selective killing of cancer cells by Ashwagandha leaf extract and its component Withanone involves ROS signaling, PLoS One 5 (10) (2010), e13536.

[42] R. Gao, N. Shah, J.S. Lee, S.P. Katiyar, L. Li, E. Oh, D. Sundar, C.O. Yun, R. Wadhwa, S.C. Kaul, Withanone-rich combination of Ashwagandha withanolides restricts metastasis and angiogenesis through hnRNP-K, Mol. Cancer Ther. 13 (12) (2014) 2930–2940.

[43] P. Bhargava, V. Malik, Y. Liu, J. Ryu, S.C. Kaul, D. Sundar, R. Wadhwa, Molecular insights into Withaferin-A-induced senescence: bioinformatics and experimental evidence to the role of NFkappaB and CARF, J. Gerontol. A Biol. Sci. Med. Sci. 74 (2) (2019) 183–191.

[44] V. Kumar, J.K. Dhanjal, P. Bhargava, A. Kaul, J. Wang, H. Zhang, S.C. Kaul, R. Wadhwa, D. Sundar, Withanone and Withaferin-A are predicted to interact with transmembrane protease serine 2 (TMPRSS2) and block entry of SARS-CoV-2 into cells, J. Biomol. Struct. (2020) 1–13.

[45] D.E. Afar, I. Vivanco, R.S. Hubert, J. Kuo, E. Chen, D.C. Saffran, A.B. Raitano, A. Jakobovits, Catalytic cleavage of the androgen-regulated TMPRSS2 protease results in its secretion by prostate and prostate cancer epithelia, Cancer Res. 61 (4) (2001) 1686–1692.

[46] Schrödinger, Glide, LigPrep, Protein Preparation Wizard, Prime, Desmond Molecular Dynamics System, Maestro-Desmond Interoperability Tools, Schrödinger, LLC, New York, NY, 2020.

[47] E. Harder, W. Damm, J. Maple, C. Wu, M. Reboul, J.Y. Xiang, L. Wang, D. Lupyan, M.K. Dahlgren, J.L. Knight, J.W. Kaus, D.S. Cerutti, G. Krilov, W.L. Jorgensen, R. Abel, R.A. Friesner, OPLS3: a force field providing broad coverage of drug-like small molecules and proteins, J. Chem. Theory Comput. 12 (1) (2016) 281–296.

[48] G. Madhavi Sastry, M. Adzhigirey, T. Day, R. Annabhimoju, W. Sherman, Protein and ligand preparation: parameters, protocols, and influence on virtual screening enrichments, J. Comput. Aided Mol. Des. 27 (3) (2013) 221–234.

[49] J.R. Greenwood, D. Calkins, A.P. Sullivan, J.C. Shelley, Towards the comprehensive, rapid, and accurate prediction of the favorable tautomeric states of drug-like molecules in aqueous solution, J. Comput. Aided Mol. Des. 24 (6–7) (2010) 591–604.

[50] A. Paoloni-Giacobino, H. Chen, M.C. Peitsch, C. Rossier, S.E. Antonarakis, Cloning of the TMPRSS2 gene, which encodes a novel serine protease with transmembrane,

[51] LDLRA, and SRCR domains and maps to 21q22.3, Genomics 44 (3) (1997) 309–320.

[51] S. Wilson, B. Greer, J. Hooper, A. Zijlstra, B. Walker, J. Quigley, S. Hawthorne, The membrane-anchored serine protease, TMPRSS2, activates PAR-2 in prostate cancer cells, Biochem. J. 388 (Pt 3) (2005) 967–972.

[52] R.A. Friesner, R.B. Murphy, M.P. Repasky, L.L. Frye, J.R. Greenwood, T.A. Halgren, P.C. Sanschagrin, D.T. Mainz, Extra precision glide: docking and scoring incorporating a model of hydrophobic enclosure for protein-ligand complexes, J. Med. Chem. 49 (21) (2006) 6177–6196.

[53] K.J. Bowers, D.E. Chow, H. Xu, R.O. Dror, M.P. Eastwood, B.A. Gregersen, J.L. Klepeis, I. Kolossvary, M.A. Moraes, F.D. Sacerdoti, Scalable algorithms for molecular dynamics simulations on commodity clusters, in: SC'06: Proc. 2006 ACM/IEEE Conference on Supercomputing, IEEE, 2006, p. 43.

[54] R.C. Wade, P.J. Goodford, The role of hydrogen-bonds in drug binding, Prog. Clin. Biol. Res. 289 (1989) 433–444.

[55] M.P. Jacobson, D.L. Pincus, C.S. Rapp, T.J. Day, B. Honig, D.E. Shaw, R.A. Friesner, A hierarchical approach to all-atom protein loop prediction, Proteins 55 (2) (2004) 351–367.

[56] F. Wang, C. Chen, W. Tan, K. Yang, H. Yang, Structure of main protease from human coronavirus NL63: insights for wide spectrum anti-coronavirus drug design, Sci. Rep. 6 (1) (2016) 22677.

[57] S. Garg, H. Huifu, S.C. Kaul, R. Wadhwa, Integration of conventional cell viability assays for reliable and reproducible read-outs: experimental evidence, BMC Res. Notes 11 (1) (2018) 403.

[58] M. Dong, J. Zhang, X. Ma, J. Tan, L. Chen, S. Liu, Y. Xin, L. Zhuang, ACE2, TMPRSS2 distribution and extrapulmonary organ injury in patients with COVID-19, Biomed. Pharmacother. 131 (2020), 110678.

[59] W. Sungnak, N. Huang, C. Becavin, M. Berg, R. Queen, M. Litvinukova, C. Talavera-Lopez, H. Maatz, D. Reichart, F. Sampaziotis, K.B. Worlock, M. Yoshida, J.L. Barnes, H.C.A.L.B., Network, SARS-CoV-2 entry factors are highly expressed in nasal epithelial cells together with innate immune genes, Nat. Med. 26 (5) (2020) 681–687.

[60] S.C. Kaul, Y. Ishida, K. Tamura, T. Wada, T. Iitsuka, S. Garg, M. Kim, R. Gao, S. Nakai, Y. Okamoto, K. Terao, R. Wadhwa, Novel methods to generate active ingredients-enriched Ashwagandha leaves and extracts, PLoS One 11 (12) (2016), e0166945.

[61] A. Kaur, B. Singh, P. Ohri, J. Wang, R. Wadhwa, S.C. Kaul, P.K. Pati, A. Kaur, Organic cultivation of Ashwagandha with improved biomass and high content of active withanolides: use of vermicompost, PLoS One 13 (4) (2018), e0194314.

[62] J.S. Mani, J.B. Johnson, J.C. Steel, D.A. Broszczak, P.M. Neilsen, K.B. Walsh, M. Naiker, Natural product-derived phytochemicals as potential agents against coronaviruses: a review, Virus Res. 284 (2020), 197989.

[63] I.E. Orhan, F.S. Senol Deniz, Natural products as potential leads against coronaviruses: could they be encouraging structural models against SARS-CoV-2? Nat. Prod. Bioprospect. 10 (4) (2020) 171–186.

[64] I.L. Paraiso, J.S. Revel, J.F. Stevens, Potential use of polyphenols in the battle against COVID-19, Curr. Opinion Food Sci. 32 (2020) 149–155.

[65] M. Russo, S. Moccia, C. Spagnuolo, I. Tedesco, G.L. Russo, Roles of flavonoids against coronavirus infection, Chem. Biol. Interact. 328 (2020), 109211.

[66] R.V. Chikhale, S.S. Gurav, R.B. Patil, S.K. Sinha, S.K. Prasad, A. Shakya, S.K. Shrivastava, N.S. Gurav, R.S. Prasad, Sars-cov-2 host entry and replication inhibitors from indian ginseng: an in-silico approach, J. Biomol. Struct. Dynam. (2020) 1–12.

[67] M.K. Tripathi, P. Singh, S. Sharma, T.P. Singh, A.S. Ethayathulla, P. Kaur, Identification of bioactive molecule from Withania somnifera (Ashwagandha) as SARS-CoV-2 main protease inhibitor, J. Biomol. Struct. Dynam. (2020) 1–14.